Materials and Design 202 (2021) 109548

Contents lists available at ScienceDirect

Materials and Design

journal homepage: www.elsevier.com/locate/matdes

Design and development of Ti–Zr–Hf–Nb–Ta–Mo high-entropy alloys for metallic biomaterials

Yuuka Iijima [a], Takeshi Nagase [a,b], Aira Matsugaki [a], Pan Wang [c], Kei Ameyama [d], Takayoshi Nakano [a,*]

[a] Division of Materials and Manufacturing Science, Graduate School of Engineering, Osaka University, 2-1 Yamadaoka, Suita 565-0871, Japan
[b] Research Center for Ultra-High Voltage Electron Microscopy, Osaka University, 7-1 Mihogaoka, Ibaraki 567-0047, Japan
[c] Singapore Institute of Manufacturing Technology, A*STAR, 73 Nanyang Drive, 637662, Singapore
[d] Department of Mechanical Engineering, Ritsumeikan University, 1-1-1 Noji-higashi, Kusatsu 525-8577, Japan

HIGHLIGHTS

- Alloy design of high-entropy alloys for metallic biomaterials (BioHEAs) was proposed.
- New alloy parameters of Mo equivalent for BioHEAs were introduced.
- Alloy design contains the prediction based on ab initio calculation database.
- Alloy design includes thermodynamic calculation.
- Ti–Zr–Hf–Nb–Ta–Mo BioHEA with room-temperature ductility was developed.

GRAPHICAL ABSTRACT

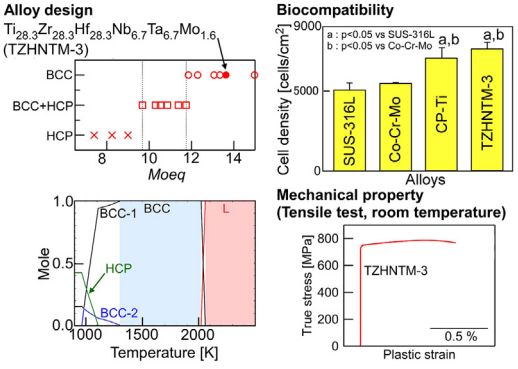

ARTICLE INFO

Article history:
Received 29 October 2020
Received in revised form 17 January 2021
Accepted 2 February 2021
Available online 5 February 2021

Keywords:
Alloy design
High-entropy alloys
Biomaterials
Thermodynamic calculation
Solidification
Biocompatibility

ABSTRACT

Applying empirical alloy parameters (including Mo equivalent), the predicted ground state diagram, and thermodynamic calculations, noble nonequiatomic Ti–Zr–Hf–Nb–Ta–Mo high-entropy alloys for metallic biomaterials (BioHEAs) were designed and newly developed. It is found that the Moeq and valence electron concentration (VEC) parameters are useful for alloy design involving BCC structure formation in bio medium-entropy alloys and BioHEAs. Finally, we find a $Ti_{28.33}Zr_{28.33}Hf_{28.33}Nb_{6.74}Ta_{6.74}Mo_{1.55}$ (at.%) BioHEA that exhibits biocompatibility comparable to that of CP–Ti, higher mechanical strength than CP–Ti, and an appreciable room-temperature tensile ductility. The current findings pave the way for new Ti–Zr–Hf–Nb–Ta–Mo BioHEAs development and are applicable for another BioHEA alloys system.

1. Introduction

New metallic biomaterials that simultaneously exhibit superior biocompatibility and mechanical properties are necessary to meet the future demands of the medical field. Recently, a new class of structural and functional materials called high-entropy alloys (HEAs) has been developed [1–5]. HEAs for metallic biomaterials, called BioHEAs, have been developed in various alloy systems: Ti–Nb–Ta–Zr–Mo [6–10], Ti–Zr–Hf–Nb–Ta–Mo [11,12], Ti–Zr–Nb–Ta–Fe [13], Ti–Zr–Hf–Cr–Mo [14], and Ti–Zr–Hf–Co–Cr–Mo [14]. The constituent elements in BioHEAs are similar to those in refractory high-entropy alloys (RHEAs) [15–17]; however, the concept of alloy design and desired properties in BioHEAs significantly differ from RHEAs. The mechanical properties

* Corresponding author.
E-mail address: nakano@mat.eng.osaka-u.ac.jp (T. Nakano).

https://doi.org/10.1016/j.matdes.2021.109548

including the creep resistance, the phase stability of BCC phase, and the oxidation resistance at high temperature regions, were important for RHEAs. In contrast, biocompatibility and the mechanical properties at room temperature were dominant factors for BioHEAs. Furthermore, enhancing the room-temperature ductility in BioHEAs is exceedingly crucial for their development. RHEAs are known to exhibit poor room-temperature ductility [17–19]. Several studies have attempted to overcome room-temperature ductility; however the reason for poor room-temperature ductility remains unclear. This characteristic is similar to those of BioHEAs, and this may correspond to the similarity in the constituent elements between RHEAs and BioHEAs.

HEAs are multicomponent alloys comprising five or more constituent elements. Their compositional complexity hinders alloy design, especially the elucidation of suitable alloy compositions. Various alloy parameters for predicting the solid solution formation tendency in multicomponent alloys have already been suggested and applied to alloy design in HEAs [4,5]. Furthermore, thermodynamic and ab initio calculations was employed in attempt to design alloys in HEAs [4,5]. We suggested an alloy design using the ground state diagrams predicted by Materials Projects [20,21] for designing multicomponent alloys, including metallic glasses [22] and HEAs [23–25]. We also demonstrated that thermodynamic calculations were effective in predicting the constituent phases in BioHEAs [8–10,14]. In the present study, alloy design concepts based on the combination of empirical alloy parameters, including newly suggested parameters, predicted ground state diagrams, and thermodynamic calculations were investigated. Furthermore, the first development of new Ti–Zr–Hf–Nb–Ta–Mo BioHEAs that exhibits biocompatibility comparable to that of CP–Ti, higher mechanical strength than CP–Ti, and an appreciable room-temperature tensile ductility, was reported.

2. Alloy design

Equiatomic TiZrHfNbTaMo HEA — $Ti_{16.67}Zr_{16.67}Hf_{16.67}Nb_{16.67}Ta_{16.67}Mo_{16.67}$, at.% (TZHNTM-Eq) — was selected as the starting alloy because of its superior mechanical strength and good compressive ductility [26–28]. In the present study, nonequiatomic Ti–Zr–Hf–Nb–Ta–Mo BioHEAs was designed and developed. The Ti–Zr–Hf–Nb–Ta–Mo alloy system is a combination of Ti–Zr–Nb–Ta–Mo BioHEAs and Hf. Hf is a metallic element with good biocompatibility, as confirmed by animal implantation tests [29]. Moreover, Hf has been used as an additive element in Ti-based biomaterials [30,31]. To enhance the room-temperature ductility in BioHEAs, three strategies were considered: [1] attaining the mixing entropy of $\Delta S_{mix} \geq 1.5\ R$ for satisfying the entropy-based definition of HEAs [4,5], where ΔS_{mix} is evaluated by the mixing enthalpy of the ideal/regular solid solution and R is the gas constant, [2] decreasing the melting temperature for the suppression of casting defects such as cold shut [8], and [3] decreasing the valence electron concentration (*VEC*) based on the literature [18]. For the design of the nonequiatomic Ti–Zr–Hf–Nb–Ta–Mo alloys, $Ti_{B+Ax}Zr_{B+Ax}Hf_{B+Ax}Nb_{B+Ax}Ta_{B+Ax}Mo_{B+Ax}$ was considered, where A is a constant related to the melting temperature of a pure element, B is the constant related to the *VEC* of a pure element, and x is a valuable number. The constants A and B are dependent on the elements. To decrease the melting temperature of the alloy, the constant A was defined as $A = (T_m - T_m(i))/T_m$, where $T_m(i)$ is the melting temperature of the i-th element and $T_m = \left(\frac{1}{6}\right) \cdot \sum_{i=1}^{6} T_m(i)$ is the average melting temperature of Ti, Zr, Hf, Nb, Ta, and Mo. The constant A of each element was as follows: $A(Ti) = 0.251$, $A(Zr) = 0.167$, $A(Hf) = 0.033$, $A(Nb) = -0.062$, $A(Ta) = -0.270$, and $A(Mo) = -0.118$. In the case of $B = 1$ for all the constituent elements, the ΔS_{mix} and the compositional average melting temperature $T_m = \sum_{i=1}^{6} x_i \cdot T_m(i)$ (x_i is the mole fraction of the i-th element) decreased monotonously with an increase in x in the $Ti_{B+Ax}Zr_{B+Ax}Hf_{B+Ax}Nb_{B+Ax}Ta_{B+Ax}Mo_{B+Ax}$ alloy. The value of x was determined to minimize T_m with the satisfaction of $\Delta S_{mix} \geq 1.5\ R$, resulting in $TiZr_{0.86}Hf_{0.58}Nb_{0.40}Ta_{0.28}Mo_{0.01}$ ($Ti_{32.07}Zr_{27.58}Hf_{18.49}Nb_{12.70}Ta_{0.19}Mo_{8.97}$, at.%) (TZHNTM-1). To simultaneously decrease the $\overline{T_m}$ and *VEC* in the alloy, the constant B of each element was set as follows: $B(Ti) = 1.5$, $B(Zr) = 1.5$, $B(Hf) = 1.5$, $B(Nb) = 1.25$, $B(Ta) = 1.25$, and $B(Mo) = 1$. The *VEC* ratios among the constituent elements were the following: (Ti, Zr, Hf): (Nb, Ta): Mo = 4: 5: 6. Based on these values, the value of B was set as follows: (Ti, Zr, Hf): (Nb, Ta): Mo = 4: 5: 6 = 1.5: 1.25: 1. In the case of B(Ti, Zr, Hf) = 1.5, B(Nb, Ta) = 1.25, and $B(Mo) = 1$, the ΔS_{mix}, $\overline{T_m}$ and *VEC* decreased monotonously with an increase in x in $Ti_{B+Ax}Zr_{B+Ax}Hf_{B+Ax}Nb_{B+Ax}Ta_{B+Ax}Mo_{B+Ax}$ alloy. The value of x was determined to minimize the $\overline{T_m}$ and *VEC* while satisfying $\Delta S_{mix} \geq 1.5\ R$, resulting in $TiZr_{0.88}Hf_{0.63}Nb_{0.37}Ta_{0.24}Mo_{0.02}$ ($Ti_{32.61}Zr_{28.58}Hf_{20.39}Nb_{12.05}Ta_{0.80}Mo_{5.57}$, at.%) (TZHNTM-2). To minimize the *VEC* without considering the $\overline{T_m}$, $Ti_{x1}Zr_{x1}Hf_{x1}Nb_{x2}Ta_{x2}Mo_{x3}$ was considered, where $x1$, $x2$, and $x3$ are variable numbers, the values of *VEC* in Ti, Zr, Hf ($x1$) are the same, and those in Nb and Ta ($x2$) are the same, and that of Mo ($x3$) is different from those of Ti, Zr, Hf, Nb, and Ta. With the satisfaction of $\Delta S_{mix} \geq 1.5\ R$, $x1$, $x2$, and $x3$ were decided as 1, 0.24, and 0.05 to minimize the *VEC* in $Ti_{x1}Zr_{x1}Hf_{x1}Nb_{x2}Ta_{x2}Mo_{x3}$, resulting in $TiZrHfNb_{0.24}Ta_{0.24}Mo_{0.05}$ ($Ti_{28.33}Zr_{28.33}Hf_{28.33}Nb_{6.74}Ta_{6.74}Mo_{1.55}$, at.%) (TZHNTM-3). The empirical alloy parameters ΔH_{mix} [4,5], $\delta(\Delta H_{mix})$ [32], Ω [4,5], and δ [4,5] for predicting solid solution formation tendency are shown in Table 1. The equations of ΔH_{mix}, $\delta(\Delta H_{mix})$, Ω, and δ parameters are written as follows:

$$\Delta H_{mix} = 4\sum_{i}\sum_{j,j\neq i} x_i \cdot x_j \cdot \Delta H_{i-j}, \tag{1}$$

$$\delta(\Delta H_{mix}) = 4\sum_{i}\sum_{j,j\neq i} x_i \cdot x_j \cdot \left|\Delta H_{mix} - \Delta H_{i-j}\right|, \tag{2}$$

$$\Omega = \frac{T_m \cdot \Delta S_{mix}}{|\Delta H_{mix}|}, \tag{3}$$

and

$$\delta = \sqrt{\sum_{i} 1 - x_i \cdot \left(\frac{r_i}{\bar{r}}\right)^2}, \tag{4}$$

where $\bar{r}$ is the compositional average of the atomic radius of the constituent elements ($\bar{r} = \sum_{i=1}^{6} x_i \cdot r_i$). The values of $\Delta H_{i\text{-}j}$ and r_i were obtained from literature [33,34]. The mixing enthalpy ΔH_{mix} corresponds to the compositional average of the $\Delta H_{i\text{-}j}$ of constituent elements in the multicomponent alloys, while $\delta(\Delta H_{mix})$ can be evaluated as the deviation of $\Delta H_{i\text{-}j}$ among constituent elements. Meanwhile, Ω is a nondimensional parameter that includes ΔS_{mix} and ΔH_{mix}. The difference in the atomic size of the constituent elements in multicomponent alloys can be evaluated using δ; however, these cannot be discussed using ΔH_{mix}, $\delta(\Delta H_{mix})$, and Ω. The empirical alloy parameters in Table 1 indicate the high solid solution formation tendency in equiatomic TiZrHfNbTaMo (TZHNTM-Eq) and nonequiatomic Ti–Zr–Hf–Nb–Ta–Mo (TZHNTM-X, X = 1, 2, 3).

Table 1
Empirical alloy parameters of equiatomic TiZrHfNbTaMo (TZHNTM-Eq) and nonequiatomic Ti–Zr–Hf–Nb–Ta–Mo (TZHNTM-X, X = 1, 2, 3).

Alloys	$\Delta S_{mix}/R$	ΔH_{mix}	$\delta(\Delta H_{mix})$	Ω	δ	*VEC*	*Moeq*
TZHNTM-Eq	1.79	−1.0	5.33	36.0	6.35	4.67	32.1
TZHNTM-1	1.52	−0.43	2.44	73.3	5.91	4.22	17.0
TZHNTM-2	1.50	0.25	2.44	113	5.62	4.21	16.3
TZHNTM-3	1.50	0.99	2.19	28.0	5.17	4.17	13.6

We have further predicted of the solid solution formation tendency and the constituent phases in the ingots based on the new alloy parameters, ground state diagram precited from the database of the first-principle calculations, and CALculation of PHAse Diagram (CALPHAD), as shown in Figs. 1-5. It was reported that the *VEC* was effective for predicting the phase stability of BCC/HCP [35] and the ductility in the ingots [18]. The Mo equivalent (*Moeq*) was widely used for the alloy design in Ti-based alloys [36–38]. Recently, Ishida suggested a new *Moeq* based on the thermodynamic database of the Ti alloys [39], as shown in Eq. (5) [39].

$$\begin{aligned}\text{Moeq} = {} & [\text{Mo}] + 0.26[\text{Au}] + 0.43[\text{Bi}] + 12.62[\text{Be}] + 2.93[\text{Co}] \\ & + 1.65[\text{Cr}] + 0.85[\text{Cu}] + 4.17[\text{Fe}] + 0.05[\text{Hf}] + 0.17[\text{Mg}] \\ & + 3.28[\text{Mn}] + 0.64[\text{Nb}] + 1.75[\text{Ni}] + 0.23[\text{Os}] + 0.71[\text{Pd}] \\ & + 0.64[\text{Pt}] + 0.29[\text{Pu}] + 1.72[\text{Re}] + 2.89[\text{Rh}] + 1.67[\text{Ru}] \\ & + 0.97[\text{Si}] + 0.23[\text{Ta}] + 0.32[\text{U}] + 0.80[\text{V}] + 0.56[\text{W}] \\ & + 1.13[\text{Y}] + 0.16[\text{Zr}], \end{aligned} \quad (5)$$

where [M] denotes the weight percent of the element M. It should be noted that the *Moeq* shown in Eq. (5) can be used for multicomponent alloys including RHEAs and BioHEAs with Ti, Zr, and Hf (4-group elements), V, Nb, and Ta elements (5-group elements), and Cr, Mo, and W elements (6-group elements). In the other word, the new *Moeq* containing more elements is potentially useful for a design guideline of multicomponent alloys. In the present study, we firstly apply the new *Moeq* (Eq. (5) and the *VEC* for new alloy design to predict the phase stability of BCC/HCP phases in medium-entropy alloys (MEAs) for biomedical applications (BioMEAs) and BioHEAs. In Table 1, the values of the *VEC* and *Moeq* in TZHNTM-X (X = Eq, 1, 2, 3) are given, along with the other empirical alloy parameters ΔH_{mix}, $\delta(\Delta H_{mix})$, Ω, and δ. Fig. 1 shows the prediction of BCC (○ and ●), BCC + HCP (□), and HCP (×) structures based on the *VEC* and *Moeq* in BioMEAs and BioHEAs reported to date (○, □, ×) [6–14], and TZHNTM-X (X = Eq, 1, 2, 3)(●). The constituent phases in BioMEAs and BioHEAs changed from BCC, BCC + HCP, and HCP with a decrease in the *VEC* (Fig. 1a) and *Moeq* (Fig. 1b1 and a2). The overlap of the BCC + HCP and BCC regions was observed in Fig. 1a

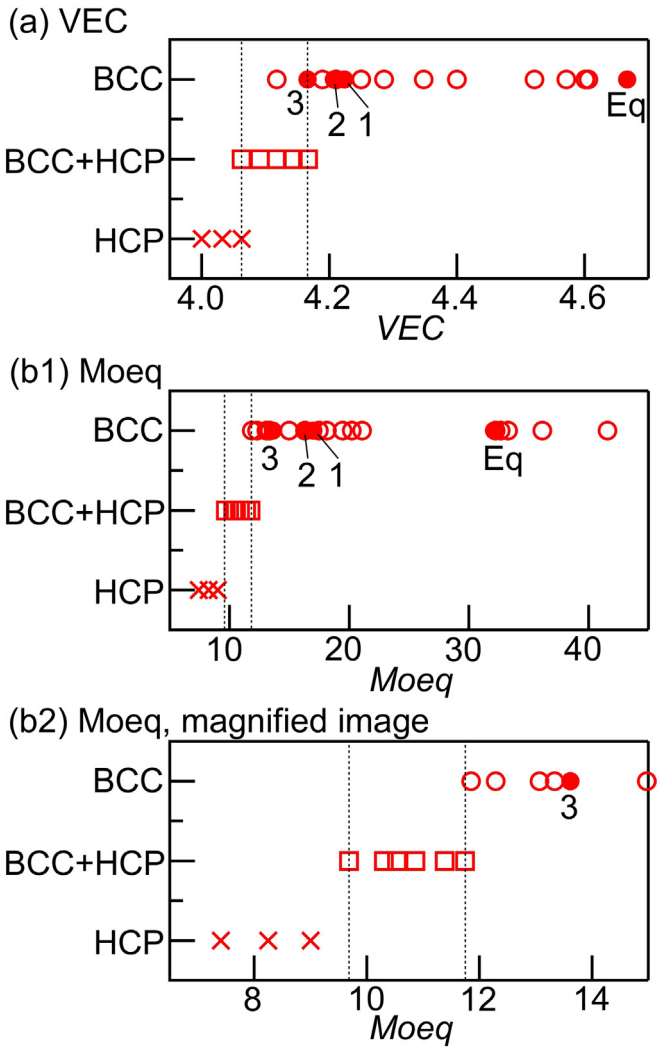

Fig. 1. Alloy design for predicting BCC and HCP phases in BioMEAs and BioHEAs including Ti–Zr–Hf–Nb–Ta–Mo BioHEAs. (a) *VEC* parameter and (b) *Moeq* parameter. (b2) is the magnified image of (b1). The indices Eq, 1, 2, and 3 denote TZHNTM-X (X = Eq, 1, 2, 3), respectively.

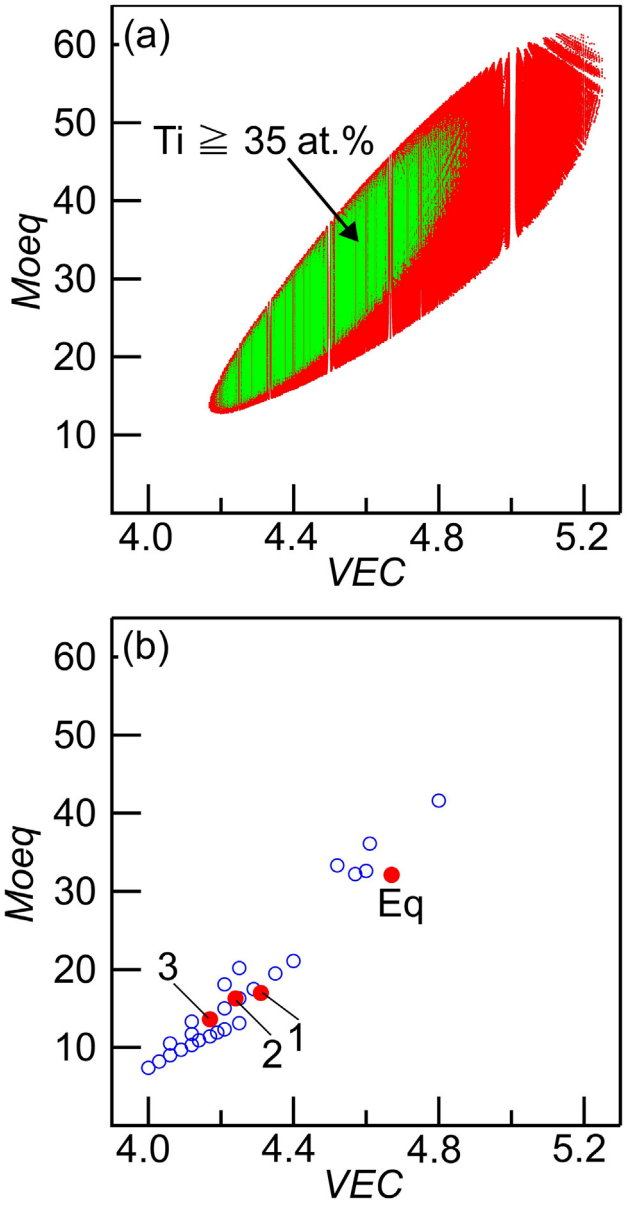

Fig. 2. Relationship between the *VEC* and *Moeq* parameters. (a) Ti–Zr–Hf–Nb–Ta–Mo alloys with $\Delta S_{mix} \geq 1.5\ R$, (b) BioMEAs and BioHEAs including Ti–Zr–Hf–Nb–Ta–Mo alloys. In Fig. 2a, the green dot indicates the alloys whose Ti concentration was at and above 35 at.% as the Ti-rich alloys. In Fig. 2b, hollow blue circles (○) and red closed circles (●) indicate Ti–Zr–Hf–Nb–Ta–Mo alloy investigated in the present study, and the indices Eq, 1, 2, and 3 denote the TZHNTM-X (X = Eq, 1, 2, 3), respectively.

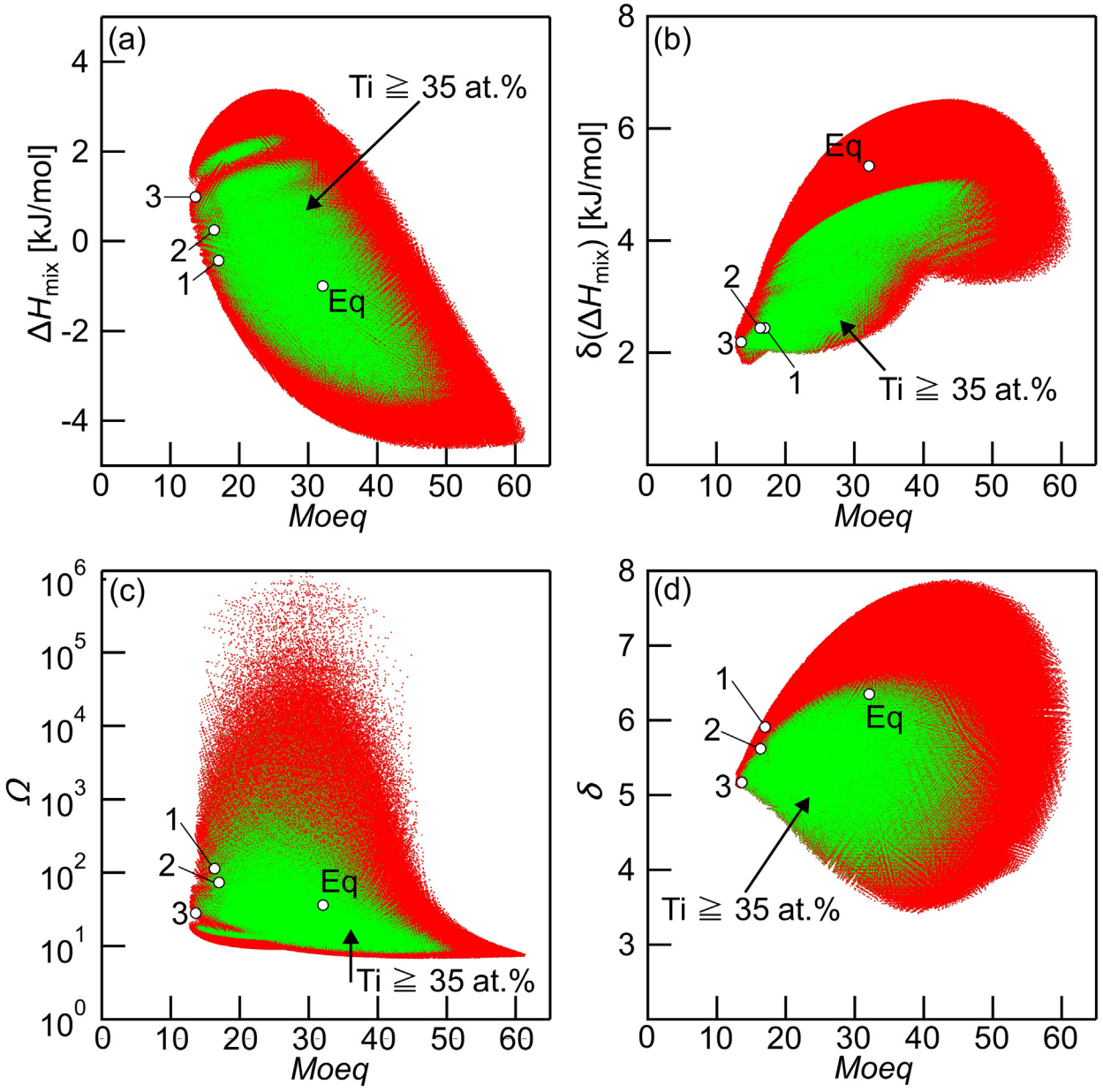

Fig. 3. Relationship between the *Moeq* and various empirical alloy parameters for predicting solid solution formation including ΔH_{mix}, $\delta(\Delta H_{mix})$, Ω, and δ parameters in Ti–Zr–Hf–Nb–Ta–Mo alloys with $\Delta S_{mix} \geq 1.5\ R$ (red dots). The green dot indicates the alloys whose Ti concentration was at and above 35 at.% and considered the Ti-rich alloys. Hollow black circles (○) indicate the Ti–Zr–Hf–Nb–Ta–Mo alloy investigated in the present study. (a) *Moeq* vs. ΔH_{mix}, (b) *Moeq* vs. $\delta(\Delta H_{mix})$, (c) *Moeq* vs. Ω, (d) *Moeq* vs. δ parameters.

when *VEC* was used, while the overlap was not observed in Fig. 1b1 and b2 using *Moeq*. The *Moeq* and *VEC* were effective in predicting the phase stability of BCC/HCP in BioMEAs and BioHEAs.

Fig. 2 shows the relationship between the *VEC* and *Moeq* values of BioMEAs and BioHEAs, including Ti–Zr–Hf–Nb–Ta–Mo alloys. Fig. 2a shows the *VEC* and *Moeq* values of Ti–Zr–Hf–Nb–Ta–Mo alloys with $\Delta S_{mix} \geq 1.5\ R$, where approximately 1.5×10^7 combinations of compositions were calculated. The red and green dots denote the alloys satisfying the condition $\Delta S_{mix} \geq 1.5R$. The green region contains the alloys with $\Delta S_{mix} \geq 1.5R$ and those alloys with Ti mole fraction (x_{Ti}) equal to or exceeding 0.35 ($x_{Ti} \geq 0.35$), indicating the Ti-rich alloys in the multicomponent Ti–Zr–Hf–Nb–Ta–Mo alloys with $\Delta S_{mix} \geq 1.5R$. The *VEC* and *Moeq* did not exhibit a one-to-one correspondence. There was a weak relationship between the *VEC* and *Moeq* in the Ti–Zr–Hf–Nb–Ta–Mo alloys with $\Delta S_{mix} \geq 1.5R$—the *Moeq* value roughly increased with an increase in the value of *VEC*. Fig. 2b shows the relationship between the *VEC* and *Moeq* values in BioMEAs and BioHEAs reported to date (○) [6–14] and TZHNTM-X (X = Eq, 1, 2, 3)(●). The *VEC* and *Moeq* values exhibited a rough positive interaction. It is noteworthy that the *VEC* and *Moeq* did not exhibit a one-to-one correspondence in alloys which were developed as BioMEAs and BioHEAs. The differences between Ti, Zr, and Hf (4-group elements), V, Nb, and Ta elements (5-group elements), and Cr, Mo, and W elements (6-group elements) for the phase stability of BCC phase can be discussed on the basis of *Moeq* but not *VEC*. Thus, *Moeq* was considered to be effective for the alloy design and prediction of BioHEAs and BioMEAs.

We also discussed the relationship between the *Moeq* and empirical alloy parameters for predicting solid solution formation tendency (ΔH_{mix}, $\delta(\Delta H_{mix})$ Ω, δ). Fig. 3 shows the calculated results of approximately 1.5×10^7 combinations of compositions, where the red and green dots denote the Ti–Zr–Hf–Nb–Ta–Mo alloys with $\Delta S_{mix} \geq 1.5R$. Approximately 1.5×10^7 combinations of compositions were calculated.

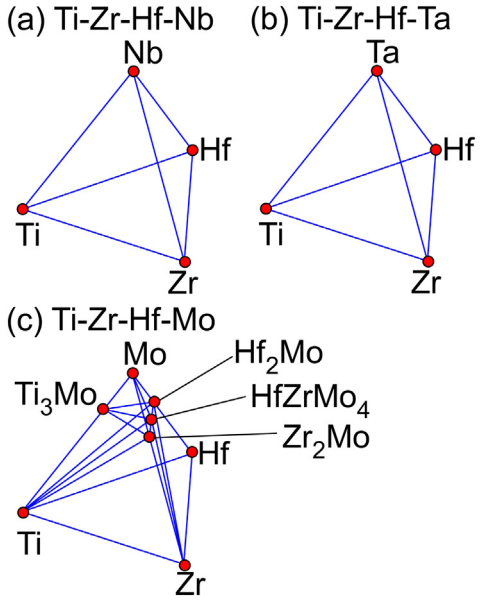

Fig. 4. Ground state diagrams in quaternary Ti–Zr–Hf–M (M = Nb, Ta, Mo) alloy systems constructed by Materials Project. (a) Ti–Zr–Hf–Nb, (b) Ti–Zr–Hf–Ta, (c) Ti–Zr–Hf–Mo.

The green region contains the alloys with $\Delta S_{mix} \geq 1.5R$ and $x_{Ti} \geq 0.35$. TZHNTM-X (X = Eq, 1, 2, 3) is indicated by the black open circles (○). There is no clear correlation between the *Moeq* and the empirical alloy parameters, and *Moeq* can be treated as an independent parameter from the other empirical alloy parameters, as well as *VEC*. Focusing on the solid solution formation tendency in Ti–Zr–Hf–Nb–Ta–Mo alloys with $\Delta S_{mix} \geq 1.5R$, the parameters ΔH_{mix} (Fig. 3a), $\delta(\Delta H_{mix})$ (Fig. 3b), and Ω (Fig. 3c) indicate the high solid solution formation tendency in Ti–Zr–Hf–Nb–Ta–Mo alloys with $\Delta S_{mix} \geq 1.5R$ regardless of the alloy composition: specifically, the low absolute value of ΔH_{mix} satisfying $-5 \leq \Delta H_{mix} \leq 5$, low value of $\delta(\Delta H_{mix})$ satisfying $\delta(\Delta H_{mix}) \leq 10$, and high value of Ω satisfying $\Omega \geq 1.1$. In Fig. 3d, some Ti–Zr–Hf–Nb–Ta–Mo alloys with $\Delta S_{mix} \geq 1.5R$ show high δ values of $\delta \geq 6.6$. This indicates that δ value must be considered for the alloy design in Ti–Zr–Hf–Nb–Ta–Mo alloy system with $\Delta S_{mix} \geq 1.5R$. No significant relationship between δ and *Moeq* means that the *Moeq* cannot be used for the alloy parameters to decrease the value of δ.

Fig. 4 shows the ground state diagram constructed by Materials Project [20,21]. The quaternary phase diagrams in Fig. 4 were not constructed by the thermodynamic calculation based on the thermodynamic data, but by the ab-initio calculations. The ground state diagrams were constructed by the database of the first-principle calculations. The ambient temperature data cannot be obtained by the first-principle calculations, resulting in the ground state diagrams at 0 K. In quaternary Ti–Zr–Hf–Nb (Fig. 4a) and Ti–Zr–Hf–Ta (Fig. 4b) phase diagrams, the ground state intermetallic compound was not observed. Intermetallic compounds of Ti_3Mo [40] and laves phases of $ZrMo_2$ [41], $HfMo_2$ [42], and $HfZrMo_4$ [43] were observed in the quaternary Ti–Zr–Hf–Mo (Fig. 4c) phase diagram. The formation energies of Ti_3Mo, $ZrMo_2$, $HfMo_2$, and $HfZrMo_4$ were − 12.9 kJ/mol, −12.4 kJ/mol, −15.5 kJ/mol, and − 15.0 kJ/mol, respectively. Fig. 4 indicates that the formation of these Mo-related intermetallic compounds, including laves phases, may prevent the solid solution formation in the Ti–Zr–Hf–Nb–Ta–Mo alloy system.

Fig. 5 shows the equilibrium calculation results using FactSage version 7.3 [44] and SGTE2017 [45]. There is no significant difference between the liquidus temperatures (T_L) predicted using the thermodynamic calculation and $\overline{T_m}$. A single BCC state exists as the thermal equilibrium state at the temperature below the solidus temperature (T_S), regardless of the alloy composition. The interval between the T_L and T_S in TZHNTM-Eq (Fig. 5a) is significantly larger than that in TZHNTM-X (X = 1, 2, 3) (Figs. 5b–5d). The single BCC phase is not a thermal equilibrium state at the temperature below the BCC phase's decomposition temperature (T_D). Moreover, the T_D in TZHNTM-Eq (Fig. 5a) was significantly higher than that in nonequiatomic TZHNTM-X (X = 1, 2, 3) (Figs. 5b–5d). The HCP phase was thermally stable at a considerably lower temperature than the T_D in TZHNTM-X (X = Eq, 1, 2, 3), regardless of the alloy composition. The thermodynamic calculation revealed a high tendency for the formation of a BCC phase during solidification in TZHNTM-X (X = Eq, 1, 2, 3), where the BCC phase formation was also predicted using the *Moeq* in Fig. 1. Therefore, the TZHNTM-X (X = Eq, 1, 2, 3) alloys were selected and fabricated for further validation based on the above-described alloy design and prediction.

3. Experimental procedures

Ingots in TZHNTM-X (X = Eq, 1, 2, 3) alloys were prepared by mixing lumps and shots of pure elements using arc-melting equipment (ACM—S01, DIAVAC Ltd., Japan). Ti chips (purity = 3 N), Zr wire-cut products (purity = 3 N, 5ϕ × 5 mm), Hf sponge (purity = 2 N, 2–7 mm), Nb granules (purity = 3 N, 2–5 mm), and Ta granules (purity = 3 N, 2–5 mm) were supplied by Mitsuwa Chemicals Co. Ltd., Japan [46]. Mo shots (purity = 3 N, 2 mm) were obtained from Rare Metallic Co. Ltd., Japan [47]. To ensure homogeneous distribution of constituent elements in the alloy, the alloy was melted more than 10 times and maintained in a liquid state for approximately 300 s during each melting event. The cooling rate during the arc-melting process was estimated experimentally to be approximately 2000 Ks^{-1} [8], which was roughly one order higher than that during the conventional metallic mold casting [48] and roughly three orders higher than those during the oxide-based mold cooling [49] and cold crucible levitation melting [8]. The constituent phases and solidification microstructure of the ingots were investigated using X-ray diffraction (XRD), scanning electron microscopy (SEM), and electron probe microanalysis (EPMA). Tensile testing was performed at room temperature at a nominal strain rate of 1.67×10^{-4} s^{-1} using dog-bone-shaped specimens with a length of 5 mm, a width of 1.5 mm, and a thickness of 1.2 mm. The functionality of the developed alloy TZHNTM-X (X = Eq, 1, 2, 3) as a biomaterial was evaluated by focusing on the cell adhesion activity facilitated by the molecular interaction between cells and the surface of the alloys. Before the cell culture experiments, the specimens were washed with acetone and ethanol through ultrasonication. Primary osteoblasts were isolated from neonatal mice calvariae using a sequential collagenase/trypsin digestion procedure. The obtained cells were diluted to 10,000 cells/cm^2 and seeded onto substrates. After culturing 24 h in a 5% CO_2 humidified atmosphere, the cells were fixed with methanol and stained with a 5% Giemsa aqueous solution (FUJIFILM Wako Chemicals). The osteoblasts adhered on each substrate were observed using an optical microscope (BX60, Olympus). For the visualization of the cytoskeletal organization on the fabricated specimens, the cells were fixed in 4% paraformaldehyde, washed in phosphate-buffered saline with Triton X-100, and immersed in a normal goat serum solution to block non-specific antibody binding. Following this, the cells were incubated with anti-vinculin antibodies (Sigma) and subsequently with secondary antibodies (Alexa Fluor 594 goat anti mouse IgG (Thermo Fisher Scientific), Alexa Fluor 488 phalloidin (Thermo Fisher Scientific)), and Hoechst 33342 (Nacalai Tesque, Kyoto, Japan), and mounted with ProLong Diamond reagent (Thermo Fisher Scientific). Cell images were obtained using fluorescent microscopy (BZ-X710, Keyence). The data are expressed as mean ± standard deviation. Statistical significance was assessed using one-way ANOVA followed by Tukey's post-hoc test. A significance of $p < 0.05$ was required to reject the null hypothesis. Software using in the present study were summarized in the supplementary materials.

4. Results and discussion

Fig. 6 shows the XRD patterns of arc-melted ingots of the TZHNTM-X (X = Eq, 1, 2, 3) alloys. In the XRD patterns (Fig. 6a), the calculated XRD

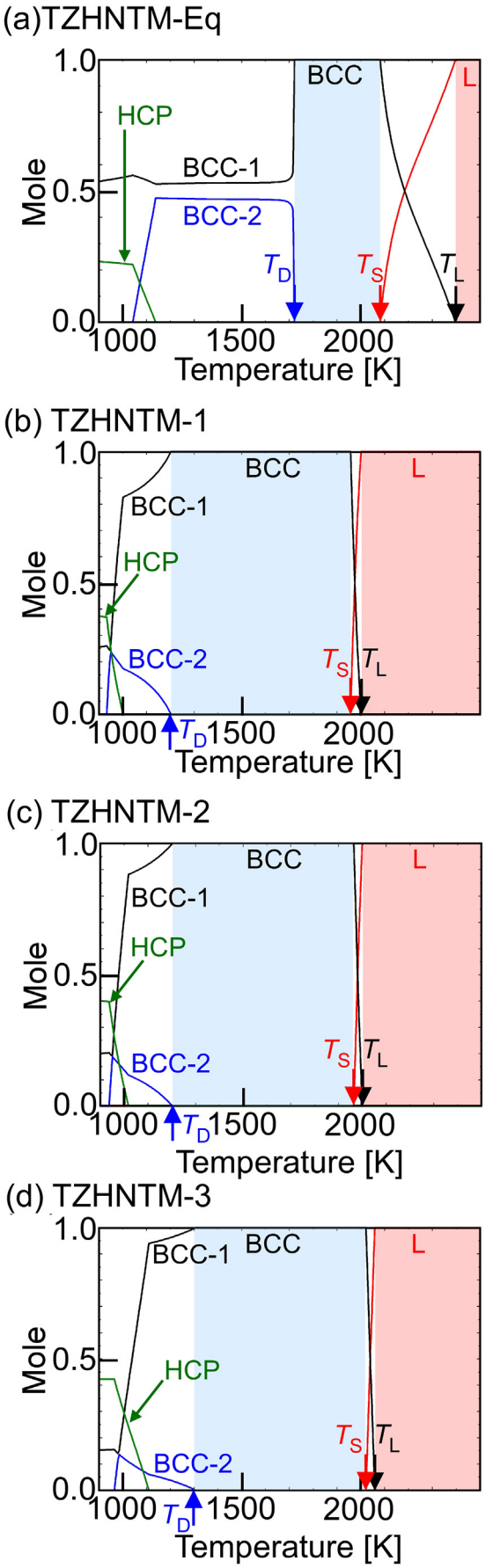

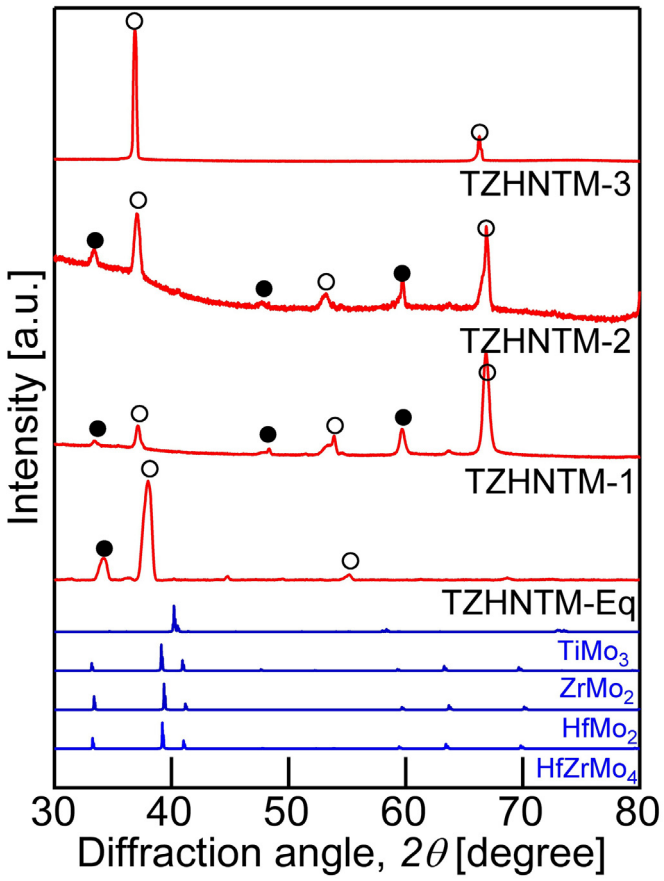

Fig. 6. XRD patterns of the arc-melted ingots of TZHNTM-X (X = Eq, 1, 2, 3) alloys together with the calculated XRD intensity of $TiMo_3$ [40], $ZrMo_2$ [41], $HfMo_2$ [42], and $HfZrMo_4$ [43] intermetallic compounds.

intensities of Ti_3Mo [40], $ZrMo_2$ [41], $HfMo_2$ [42], and $HfZrMo_4$ [43] are shown, together with the experimental data. The calculated XRD intensity curves were obtained using VESTA [50]. The peaks corresponding to Mo-related intermetallic compounds shown in Fig. 5 were not observed. The main sharp peaks in the arc-melted ingots of the equiatomic TZHNTM-Eq and nonequiatomic TZHNTM-X (X = 1, 2) were identified as dual BCC phases, as indicated by the black-filled circle (●) and the hollow black circles (○). In contrast, TZHNTM-3 was identified as a single BCC phase in the XRD pattern.

Fig. 7 shows an SEM back-scattering electron (BSE) image of the arc-melted ingots (Fig. 7a) and elemental mapping of Ti, Zr, Hf, Nb, Ta, and Mo in the equiatomic TZHNTM-Eq and TZHNTM-3 as typical examples of nonequiatomic Ti–Zr–Hf–Nb–Ta–Mo alloy (Fig. 7b). An equiaxial dendrite structure composed of white contrast dendrite and gray contrast interdendrite regions was observed in the SEM-BSE image of the TZHNTM-X (X = Eq, 1, 2, 3) alloys (Fig. 7a). In the EDS element mapping images of Ti and Zr elements (Fig. 7b), the enrichment of Ti and Zr in the interdendrite region and the enrichment of Ta in the dendrite region were observed in the equiatomic TZHNTM-Eq (Fig. 7b1, left). A significant difference in the Hf, Nb, and Mo elements between dendrite and interdendrite regions was not observed in EDS element mapping images. The dual BCC phases in the XRD patterns corresponded to the dendrite BCC and interdendrite BCC phases in TZHNTM-Eq. No significant difference in the composition of the dendrite and interdendrite regions was observed in the EDS element mapping images in the

Fig. 5. Equilibrium calculation results in TZHNTM-X (X = Eq, 1, 2, 3) alloys using FactSage and SGTE2017.

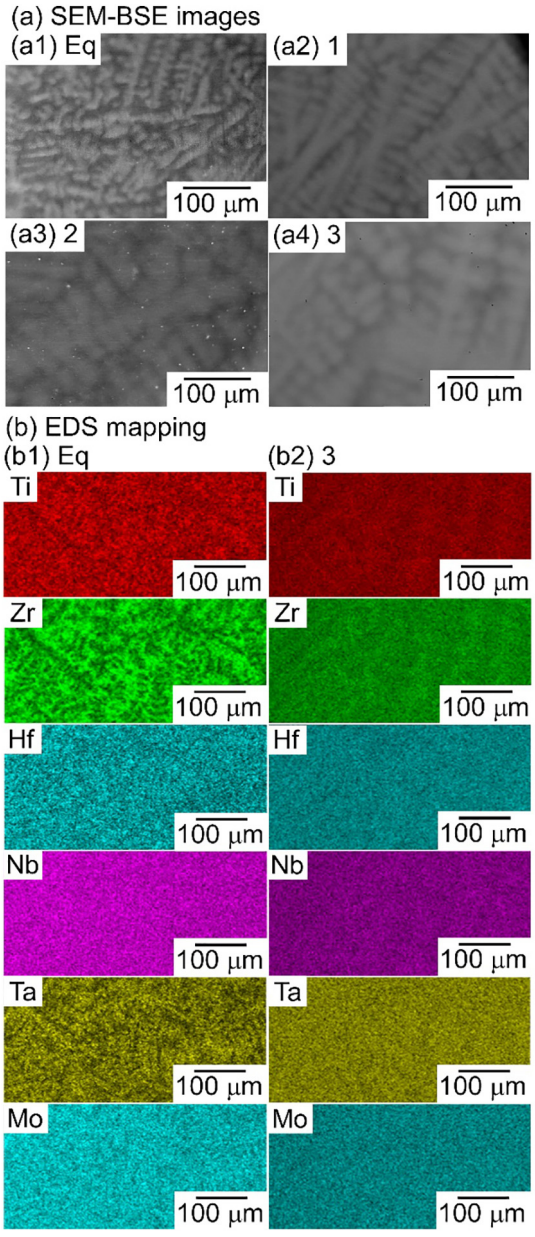

Fig. 7. Microstructure analysis of the arc-melted ingots of TZHNTM-X (X = Eq, 1, 2, 3) alloys. (a) SEM-BSE images and (b) EDS element mapping in the equiatomic TiNbTaZrMo (TZHNTM-Eq) and the nonequiatomic $Ti_{28.32}Zr_{28.32}Hf_{28.32}Nb_{6.74}Ta_{6.74}Mo_{1.55}$ (TZHNTM-3) alloys.

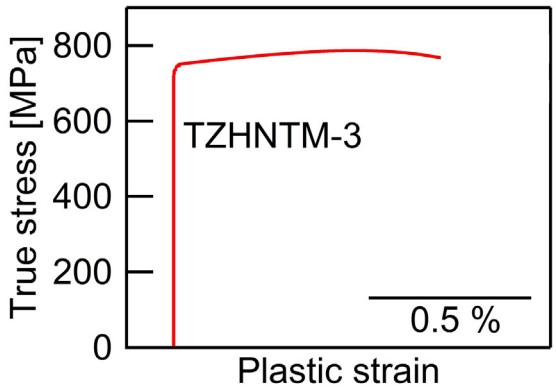

Fig. 8. True stress–plastic-strain curves from the tensile test performed at room temperature on the nonequiatomic $Ti_{28.32}Zr_{28.32}Hf_{28.32}Nb_{6.74}Ta_{6.74}Mo_{1.55}$ (TZHNTM-3) alloy.

nonequiatomic TZHNTM-3 (Fig. 7b2, right). The difference in the segregation behavior between TZHNTM-Eq and TZHNTM-3 corresponded to the thermodynamic calculation results in the interval between the T_L and T_S and the distribution coefficient at T_L (k) estimated by FactSage and SGTE2017. The distribution coefficient of Ti (k_{Ti}) and Zr (k_{Zr}) in TZHNTM-Eq were evaluated as 0.76 and 0.55, respectively. The values of k_{Ti} and k_{Zr} in TZHNTM-3 were evaluated as 0.85 and 0.93. The value of k_{Zr} in TZHNTM-Eq was under unity and considerably lower than that in TZHNTM-3. The formation of the intermetallic compounds including Mo-related compounds was not detected from XRD analysis (Fig. 6), SEM observation (Fig. 7a), and EDS mapping (Fig. 7b) in TZHNTM-X (X = Eq, 1, 2, 3).

Fig. 8 shows the mechanical property analysis results of the arc-melted ingots during the tensile test. Tensile tests at room temperature were performed on the arc-melted ingots of TZHNTM-X (X = Eq, 1, 2, 3); however, only TZHNTM-3 was available. The proof stress of TZHNTM-3 was significantly higher than that of commercial-purity Ti (CP–Ti), similar to Ti–Nb–Ta–Zr–Mo BioHEAs where the proof stress was evaluated using the compressive test [6,10]. The reason why tensile testing on arc-melted ingots was available only for TZHNTM-3 among TZHNTM-X (X = Eq, 1, 2, 3) at room temperature is not yet clear. The well-developed cold-shut was not observed in the arc-melted ingots of TZHNTM-3. It should be noted here that the values of the *VEC* and *Moeq* of TZHNTM-3 were the lowest among TZHNTM-X (X = Eq, 1, 2, 3). The relationship between the room-temperature ductility and *VEC* was discussed in another study [18]: the lower *VEC* was favorable for the fabrication of the ingots in RHEAs with room-temperature ductility. The present result implies that the alloy design strategy for decreasing the *VEC* and *Moeq* effectively enhanced the room-temperature ductility in BioMEAs and BioHEAs. The evaluation of the various mechanical properties, including the Young's modulus and fatigue properties at room temperature, is important for the application of BioHEAs as a new category of metallic biomaterials; however, arc-melted ingots include the heterogeneous distribution of the constituent elements due to solidification. The segregation of the constituent elements in BioHEAs was reported to be suppressed by additive manufacturing (AM) in Ti–Nb–Ta–Zr–Mo BioHEAs [51]. The thermomechanical process was considered to be effective in eliminating solidification segregation. Further investigation of the mechanism of room-temperature ductility and further evaluation of the mechanical properties of TZHNTM-3 using specimens prepared by AM and/or thermo-mechanical processes will be reported in future work.

Fig. 9 shows the biocompatibility evaluation results of arc-melted ingots in TZHNTM-3, together with SUS316L stainless steel [52], Co–Cr-based alloy (ASTM F1537–08) [53], because Co–Cr-based alloys [54–58] were widely used as metallic biomaterials together with pure Ti and Ti-based alloys, and CP–Ti as references. Fig. 9a shows the quantitative analysis results of the cell density evaluated by staining images of osteoblasts cultivated for 24 h on fabricated specimens with Giemsa. The adhesion properties of the cells to materials surface, a major factor mediating biocompatibility, differed drastically depending on the alloys. The cell densities on the SUS-316 L and Co–Cr–Mo metallic biomaterials were conspicuously lower than those on CP–Ti and TZHNTM-3. There was no statistical difference between CP–Ti and TZHNTM-3. Moreover, the cell morphology on a biomaterial, which exerts a direct influence on cellular events involving tissue or organ construction, produced characteristic properties between various types of alloys. Fig. 9b shows the fluorescent images of cytoskeletal components and focal adhesions of osteoblasts adhered on the fabricated specimens. The osteoblasts on SUS316L and the Co–Cr–Mo alloy were found to shrink in size with poor cytoskeletal organization. In contrast, those on TZHNTM-3 exhibited a widespread morphology with a dense network of actin fibers as

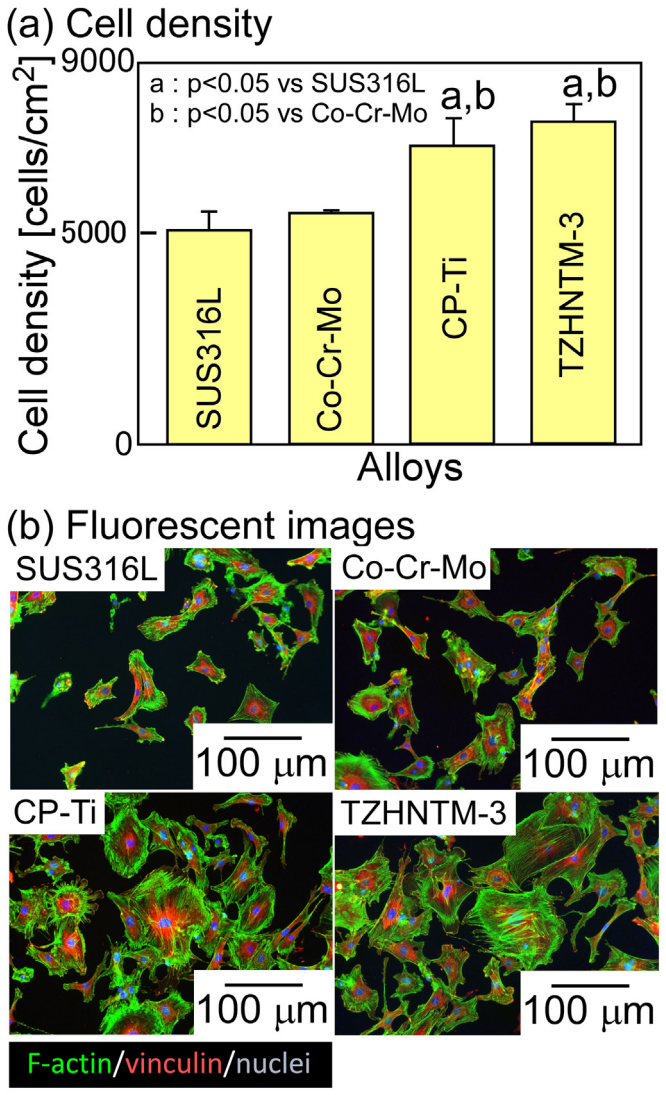

Fig. 9. Biocompatibility of the arc-melted ingots in the Ti–Zr–Hf–Nb–Ta–Mo BioHEAs of the equiatomic TiNbTaZrMo (TZHNTM-Eq) and nonequiatomic $Ti_{28.32}Zr_{28.32}Hf_{28.32}Nb_{6.74}Ta_{6.74}Mo_{1.55}$ (TZHNTM-3) BioHEAs — SUS316L stainless steel [52], Co–Cr–Mo alloy of ASTM F1537–08 [53], and commercial pure titanium (CP–Ti) were used as a reference. (a) Quantitative analysis of the density of osteoblasts cultured on the fabricated specimens by staining images with Giemsa, (b) fluorescent images of osteoblast adhesion on the fabricated specimens.

well as those on CP–Ti, which has been commonly used for orthopedic and dental implants. The results demonstrate the appropriateness of the constituent elements of the developed alloy for BioHEAs, as evidenced by their low cytotoxicity derived from excellent corrosion resistance and the formation of an oxide layer. Taken together, the developed TZHNTM-3 was found to be significantly more advantageous than SUS-316 L and the Co–Cr–Mo alloy for bone tissue compatibility, while possessing the same degree of cytocompatibility as CP–Ti, the most common metals used in BioMEAs.

The analysis of the mechanical properties by the tensile test (Fig. 8) and biocompatibility (Fig. 9) demonstrated the successful fabrication of the ingots of BioHEAs with $\Delta S_{mix} \geq 1.5\ R$, superior biocompatibility comparable to that of CP–Ti, higher mechanical strength than CP–Ti and an appreciable room-temperature tensile ductility. The alloy design with the empirical alloy parameters including *Moeq* (Eq. (5)), the predicted ground states and CALPHAD (Figs. 1-5) was effective to develop new Ti–Zr–Hf–Nb–Ta–Mo BioHEAs. The current findings pave the way for development and are applicable for another BioHEA alloys system.

5. Conclusions

In conclusion, nonequiatomic Ti–Zr–Hf–Nb–Ta–Mo BioHEAs with superior biocompatibility and mechanical properties were successfully designed and developed. The results are summarized as follows:

(1) BCC phases without intermetallic compounds were detected by the XRD patterns of the arc-melted ingots of the equiatomic $Ti_{16.67}Zr_{16.67}Hf_{16.67}Nb_{16.67}Ta_{16.67}Mo_{16.67}$ (TZHNTM-Eq) alloy and nonequiatomic $Ti_{32.07}Zr_{27.58}Hf_{18.49}Nb_{12.70}Ta_{0.19}Mo_{8.97}$ (TZHNTM-1), $Ti_{32.61}Zr_{28.58}Hf_{20.39}Nb_{12.05}Ta_{0.80}Mo_{5.57}$ (TZHNTM-2), and $Ti_{28.33}Zr_{28.33}Hf_{28.33}Nb_{6.74}Ta_{6.74}Mo_{1.55}$ (TZHNTM-3) alloys. Dual BCC phase formation was observed in the arc-melted ingots of the equiatomic $Ti_{16.67}Zr_{16.67}Hf_{16.67}Nb_{16.67}Ta_{16.67}Mo_{16.67}$ (TZHNTM-Eq) alloy, which can be explained by the differences in the chemical composition between the dendrite and interdendrite regions.

(2) In addition to the *VEC* parameter, it was found that the *Moeq* parameter was useful for the alloy design and prediction of BioMEAs and BioHEAs.

(3) Alloys design and prediction by the combination of empirical alloy parameters (including *Moeq*), the predicted ground state diagram constructed by the Materials Project, and thermodynamic calculations using the SGTE database, was effective to develop nonequiatomic Ti–Zr–Hf–Nb–Ta–Mo BioHEAs.

(4) The nonequiatomic TZHNTM-3 exhibits a significantly higher mechanical strength than CP–Ti, with good ductility for tensile testing at room temperature.

(5) The nonequiatomic TZHNTM-3 displayed superior biocompatibility, comparable to that of CP–Ti.

Declaration of Competing Interest

The authors declare that they have no known competing financial interests or personal relationships that could have appeared to influence the work reported in this paper.

The authors declare the following financial interests/personal relationships which may be considered as potential competing interests

Acknowledgments

Funding: This work was partially supported by JSPS KAKENHI (grant numbers 18H05254, 18K04750, 18H05455, 18H05256, and 19H05172) and the Innovative Design/Manufacturing Technologies Program (Establishment and Validation of the base for 3D Design & Additive Manufacturing Standing on the Concepts of "Anisotropy" & "Customization") of the New Energy and Industrial Technology Development Organization (NEDO).

Appendix A. Supplementary data

Supplementary data to this article can be found online at https://doi.org/10.1016/j.matdes.2021.109548.

References

[1] B. Cantor, I.T.H. Chang, P. Knight, A.J.B. Vincent, Microstructural development in equiatomic multicomponent alloys, Mater. Sci. Eng. A 375–377 (2004) 213–218, https://doi.org/10.1016/j.msea.2003.10.257.

[2] J.W. Yeh, S.K. Chen, S.J. Lin, J.Y. Gan, T.S. Chin, T.T. Shun, C.H. Tsau, S.Y. Chang, Nanostructured High-Entropy Alloys with Multiple Principal Elements: Novel Alloy Design Concepts and Outcomes, Adv. Eng. Mater. 6 (2004) 299–303, https://doi.org/10.1002/adem.200300567.

[3] D.B. Miracle, O.N. Senkov, A critical review of high entropy alloys and related concepts, Acta Mater. 122 (2017) 448–511, https://doi.org/10.1016/j.actamat.2016.08.081.

[4] B.S. Murty, J.-W. Yeh, S. Ranganathan, High-Entropy Alloys, first ed Elsevier, 2014https://doi.org/10.1016/C2013-0-14235-3.

[5] M.C. Gao, J.-W. Yeh, P.K. Liaw, Y. Zhang, High-Entropy Alloys, first ed Springer, 2016https://doi.org/10.1007/978-3-319-27013-5.

[6] M. Todai, T. Nagase, T. Hori, A. Matsugaki, A. Sekita, T. Nakano, Novel TiNbTaZrMo high-entropy alloys for metallic biomaterials, Scr. Mater. 129 (2017) 65–68, https://doi.org/10.1016/j.scriptamat.2016.10.028.

[7] S.P. Wang, J. Xu, TiZrNbTaMo high-entropy alloy designed for orthopedic implants: As-cast microstructure and mechanical properties, Mater. Sci. Eng. C. 73 (2017) 80–89, https://doi.org/10.1016/j.msec.2016.12.057.

[8] T. Nagase, K. Mizuuchi, T. Nakano, Solidification Microstructures of the Ingots Obtained by Arc Melting and Cold Crucible Levitation Melting in TiNbTaZr Medium-Entropy Alloy and TiNbTaZrX (X = V, Mo, W) High-Entropy Alloys, Entropy 2 (2019) 483, https://doi.org/10.3390/e21050483.

[9] T. Nagase, M. Todai, T. Hori, T. Nakano, Microstructure of equiatomic and non-equiatomic Ti-Nb-Ta-Zr-Mo high-entropy alloys for metallic biomaterials, J. Alloys Compd. 753 (2018) 412–421, https://doi.org/10.1016/j.jallcom.2018.04.082.

[10] T. Hori, T. Nagase, M. Todai, A. Matsugaki, T. Nakano, Development of non-equiatomic Ti-Nb-Ta-Zr-Mo high-entropy alloys for metallic biomaterials, Scr. Mater. 172 (2019) 83–87, https://doi.org/10.1016/j.scriptamat.2019.07.011.

[11] Y. Yuan, Y. Wu, Z. Yang, X. Liang, Z. Lei, H. Huang, H. Wang, X. Liu, K. An, W. Wu, Z. Lu, Mater. Res. Lett. 7 (2019) 225–231, https://doi.org/10.1080/21663831.2019.1584592.

[12] A. Motallebzadeh, N.S. Peighambardoust, S. Sheikh, H. Murakami, S. Guo, D. Canadinc, Formation, structure and properties of biocompatible TiZrHfNbTa high-entropy alloys, Intermetallics 113 (2019) 106572, https://doi.org/10.1016/j.intermet.2019.106572.

[13] G. Popescu, B. Ghiban, C.A. Popescu, L. Rosu, R. Trusca, I. Carcea, V. Soare, D. Dumitrescu, I. Constantin, M.T. Olaru, B.A. Carlan, New TiZrNbTaFe high entropy alloy used for medical applications, IOP Conf. Series 400 (2018) 022049, https://doi.org/10.1088/1757-899X/400/2/022049.

[14] T. Nagase, Y. Iijima, A. Matsugaki, K. Ameyama, T. Nakano, Design and fabrication of Ti–Zr-Hf-Cr-Mo and Ti–Zr-Hf-Co-Cr-Mo high-entropy alloys as metallic biomaterials, Mater. Sci. Eng. C 107 (2020) 110322, https://doi.org/10.1016/j.msec.2019.110322.

[15] O.N. Senkov, G.B. Wilks, D.B. Miracle, C.P. Chuang, P.K. Liaw, Refractory high-entropy alloys, Intermetallics 18 (2010) 1758–1765, https://doi.org/10.1016/j.intermet.2010.05.014.

[16] O.N. Senkov, J.M. Scotta, S.V. Senkova, D.B. Miracle, C.F. Woodward, Microstructure and room temperature properties of a high-entropy TaNbHfZrTi alloy, J. Alloys Compd 509 (2011) 6043–6048, https://doi.org/10.1016/j.jallcom.2011.02.171.

[17] O.N. Senkov, D.B. Miracle, K.J. Chaput, J.-P. Couzinie, Development and exploration of refractory high entropy alloys-A review, J. Mater. Res. 33 (2018) 3092–3128, https://doi.org/10.1557/jmr.2018.153.

[18] S. Sheikh, S. Shafeie, Q. Hu, J. Ahlstrom, C. Persson, J. Vesely, J. Zyka, U. Klement, S. Guo, Alloy design for intrinsically ductile refractory high-entropy alloys, J. Appl. Phys. 120 (2016) 164902, https://doi.org/10.1063/1.4966659.

[19] V. Soni, O.N. Senkov, B. Gwalani, D.B. Miracle, R. Banerjee, Microstructural Design for Improving Ductility of An Initially Brittle Refractory High Entropy Alloy, Sci. Rep. 8 (2018) 8816, https://doi.org/10.1038/s41598-018-27144-3.

[20] A. Jain, S.P. Ong, G. Hautier, W. Chen, W.D. Richards, S. Dacek, S. Cholia, D. Gunter, D. Skinner, G. Ceder, K.A. Persson, A.P.L. Materials, Commentary: The Materials Project: A materials genome approach to accelerating materials innovation, APL Materials 1 (1) (2013) 011002, https://doi.org/10.1063/1.4812323.

[21] Materials Project, https://materialsproject.org/ (Assessed, Nov. 28, 2020).

[22] T. Nagase, M. Takemura, M. Matsumuro, M. Matsumoto, Y. Fujii, Design and microstructure analysis of globules in Al-Co-La-Pb immiscible alloys with an amorphous phase, Materials & Design 117 (2017) 338–345, https://doi.org/10.1016/j.matdes.2016.12.092.

[23] T. Nagase, M. Todai, T. Nakano, Development of Ti–Zr–Hf–Y–La high-entropy alloys with dual hexagonal-close-packed structure, Scr. Mater. 186 (2020) 242–246, https://doi.org/10.1016/j.scriptamat.2020.05.033.

[24] T. Nagase, M. Todai, T. Nakano, Development of Co–Cr–Mo–Fe–Mn–W and Co–Cr–Mo–Fe–Mn–W–Ag High-Entropy Alloys Based on Co–Cr–Mo Alloys, Mater. Trans. 61 (2020) 567–576, https://doi.org/10.2320/matertrans.MT-MK2019002.

[25] T. Nagase, M. Todai, T. Nakano, Co-Cr-Cu-Fe-Mn-Ni and Co-Cr-Cu-Fe-Mn-Ni-B High Entropy Alloys for Biomedical Application, Crystals 10 (2020) 527, https://doi.org/10.3390/cryst10060527.

[26] C.-C. Juan, M.-H. Tsai, C.-W. Tsai, C.-M. Lin, W.-R. Wang, C.-C. Yang, S.-K. Chen, S.-J. Lin, J.-W. Yeh, Enhanced mechanical properties of HfMoTaTiZr and HfMoNbTaTiZr refractory high-entropy alloys, Intermetallics 62 (2015) 76–83, https://doi.org/10.1016/j.intermet.2015.03.013.

[27] C.-C. Juan, K.-K. Tseng, W.-L. Hsu, M.-H. Tsai, C.-M. Lin, S.-K. Chen, S.-J. Lin, J.-W. Yeh, Solution strengthening of ductile refractory $HfMo_xNbTaTiZr$ high-entropy alloys, Mater. Lett. 175 (2016) 284–287, https://doi.org/10.1016/j.matlet.2016.03.133.

[28] K.-K. Tseng, C.-C. Juan, S. Tso, H.-C. Chen, C.-W. Tsai, J.-W. Yeh, Nb, Ta, Ti, and Zr on Mechanical Properties of Equiatomic Hf-Mo-Nb-Ta-Ti-Zr Alloys, Entropy 21 (2019) 21, https://doi.org/10.3390/e21010015.

[29] H. Matsuno, A. Yokoyama, F. Watari, M. Uo, T. Kawasaki, Biocompatibility and osteogenesis of refractory metal implants, titanium, hafnium, niobium, tantalum and rhenium, Biomaterials 22 (2001) 1253–1262, https://doi.org/10.1016/S0142-9612(00)00275-1.

[30] B.L. Wang, L. Li, Y.F. Zheng, In vitro cytotoxicity and hemocompatibility studies of Ti-Nb, Ti-Nb-Zr and Ti-Nb-Hf biomedical shape memory alloys, Biomed. Mater. 5 (2010) 044102, https://doi.org/10.1088/1748-6041/5/4/044102.

[31] T. Hanawa, Techniques Improving Reliability of Metals in the Human Body, J. Surf. Finish. Soc. Jpn. 58 (2007) 495–499, https://doi.org/10.4139/sfj.58.495.

[32] T. Nagase, A. Terayama, T. Nagaoka, N. Fuyama, T. Sakamoto, Alloy Design and Fabrication of Ingots of Al–Mg–Li–Ca Light-Weight Medium Entropy Alloys, Mater. Trans. 61 (2020) 1369–1380, https://doi.org/10.2320/matertrans.F-M2020825.

[33] A. Takeuchi, A. Inoue, Calculations of Mixing Enthalpy and Mismatch Entropy for Ternary Amorphous Alloys, Mater. Trans. 41 (2000) 1372–1378, https://doi.org/10.2320/matertrans1989.41.1372.

[34] A. Takeuchi, A. Inoue, Classification of Bulk Metallic Glasses by Atomic Size Difference, Heat of Mixing and Period of Constituent Elements and Its Application to Characterization of the Main Alloying Element, Mater. Trans. 46 (2005) 2817–2829, https://doi.org/10.2320/matertrans.46.2817.

[35] Q.Wang Y.F.Ye, Y.Yang J.LuC.T.Liu, High-entropy alloy: challenges and prospects, materialsToday 19 (2016) 349–362, https://doi.org/10.1016/j.mattod.2015.11.026.

[36] D. Eylon, R.R. Boyer, D.A. Koss, Beta Titanium Alloys in the 1990s, TMS, Warrendale PA, 1993.

[37] G. Welsch, R. Boyer, E.W. Collings, Materials Properties Handbook: Titanium Alloys, ASM International, Materials Park, OH, 1994.

[38] P.J. Bania, Beta titanium alloys and their role in the titanium industry, JOM 46 (1994) 16–19, https://doi.org/10.1007/BF03220742.

[39] K. Ishida, Schaeffler-Type Phase Diagram of Ti-Based Alloys, Metall. Mater. Trans., A 48 (2017) 4990–4998, https://doi.org/10.1007/s11661-017-4218-3.

[40] $TiMo_3$, Materials Project ID mp-1017983, doi:10.17188/1350038

[41] $ZrMo_2$, Materials Project ID mp-2049, doi:10.17188/1195617

[42] $HfMo_2$, Materials Project ID mp-2363, doi:10.17188/1199626

[43] $HfZrMo_4$, Materials Project ID mp-1224193.

[44] FactSage, http://www.factsage.com/ (Assessed, Nov. 28, 2020).

[45] SGTE2017, http://www.crct.polymtl.ca/fact/documentation/ (Assessed, Nov. 28, 2020).

[46] Mitsuwa Chemical Co., Ltd, Japan, http://www.eonet.ne.jp/~mitsuwa-chem/index.html (Assessed, Jan. 10, 2021).

[47] RARE METALLIC Co., Ltd, Japan, http://rare-meta.co.jp/ (Assessed, Jan. 10, 2020).

[48] T. Nagase, M. Takemura, M. Matsumuro, T. Maruyama, Solidification Microstructure of $AlCoCrFeNi_{2.1}$ Eutectic High Entropy Alloy Ingots, Mater. Trans. 59 (2018) 255–264, https://doi.org/10.2320/matertrans.F-M2017851.

[49] T. Nagase, T. Kakeshita, K. Matsumura, K. Nakazawa, S. Furuya, N. Ozoe, K. Yoshino, Development of Fe-Co-Cr-Mn-Ni-C high entropy cast iron (HE cast iron) available for casting in air atmosphere, Materials & Design 184 (2019) 108172, https://doi.org/10.1016/j.matdes.2019.108172.

[50] K. Momma, F. Izumi, VESTA 3 for three-dimensional visualization of crystal, volumetric and morphology data, J. Appl. Crystallography 41 (2008) 653–658, https://doi.org/10.1107/S0021889811038970.

[51] T. Ishimoto, R. Ozasa, K. Nakano, M. Weinmann, C. Schnitter, M. Stenzel, A. Matsugaki, T. Nagase, T. Matsuzaka, M. Todai, H.S. Kim, T. Nakano, Development of TiNbTaZrMo bio–high entropy alloy (BioHEA) super–solid solution by selective laser melting, and its improved mechanical property and biocompatibility, Scr. Mater. 194 (2021) 113658, https://doi.org/10.1016/j.scriptamat.2020.113658.

[52] JIS SUS316L. http://www.jssa.gr.jp/contents/products/standards/jis/austenite/ (accessed 16 May 2019).

[53] ASTM F1537–08. https://www.astm.org/Standards/F1537.htm (accessed 16 May 2019).

[54] T.M. Devine, F.J. Kummer, J. Wulff, Wrought cobalt-chromium surgical implant alloys, J. Mater. Sci. 7 (1972) 126–128, https://doi.org/10.1007/BF00549560.

[55] T.M. Devine, J. Wulff, Cast vs. wrought cobalt-chromium surgical implant alloys, J. Biomed. Mater. Res. 9 (1975) 151–167, https://doi.org/10.1002/jbm.820090205.

[56] J. Cohen, R.M. Rose, J. Wulff, Recommended heat treatment and alloy additions for cast Co-Cr surgical implants, J. Biomed. Mater. Res. 12 (1978) 935–937, https://doi.org/10.1002/jbm.820120613.

[57] M. Niinomi, Recent metallic materials for biomedical applications, Metall. Mater. Trans. A 33 (2002) 477–486, https://doi.org/10.1007/s11661-002-0109-2.

[58] E. Liverani, A. Fortunato, A. Leardini, C. Belvedere, S. Siegler, L. Ceschini, A. Ascari, Fabrication of Co–Cr–Mo endoprosthetic ankle devices by means of Selective Laser Melting (SLM), Materials & Design 106 (2016) 60–68, https://doi.org/10.1016/j.matdes.2016.05.083.